aerospace

MDPI

Article

Aerodynamic Uncertainty Quantification of a Low-Pressure Turbine Cascade by an Adaptive Gaussian Process

Wenhao Fu , Zeshuai Chen and Jiaqi Luo *

School of Aeronautics and Astronautics, Zhejiang University, Hangzhou 310027, China; wenhaofu@zju.edu.cn (W.F.); zeshuai.chen@zju.edu.cn (Z.C.)
* Correspondence: jiaqil@zju.edu.cn

Abstract: Stochastic variations of the operation conditions and the resultant variations of the aerodynamic performance in Low-Pressure Turbine (LPT) can often be found. This paper studies the aerodynamic performance impact of the uncertain variations of flow parameters, including inlet total pressure, inlet flow angle, and turbulence intensity for an LPT cascade. Flow simulations by solving the Reynolds-averaged Navier–Stokes equations, the SST turbulence model, and $\gamma - \widetilde{Re}_{\theta t}$ transition model equations are first carried out. Then, a Gaussian process (GP) based on an adaptive sampling technique is introduced. The accuracy of adaptive GP (ADGP) is proven to be high through a function experiment. Using ADGP, the uncertainty propagation models between the performance parameters, including total pressure-loss coefficient, outlet flow angle, Zweifel number, and the uncertain inlet flow parameters, are established. Finally, using the propagation models, uncertainty quantifications of the performance changes are conducted. The results demonstrate that the total pressure-loss coefficient and Zweifel number are sensitive to uncertainties, while the outlet flow angle is almost insensitive. Statistical analysis of the flow field by direct Monte Carlo simulation (MCS) shows that flow transition on the suction side and viscous shear stress are rather sensitive to uncertainties. Moreover, Sobol sensitivity analysis is carried out to specify the influence of each uncertainty on the performance changes in the turbine cascade.

Keywords: uncertainty quantification; low-pressure turbine; Gaussian process; adaptive sampling; statistical analysis; Sobol analysis

check for updates

Citation: Fu, W.; Chen, Z.; Luo, J. Aerodynamic Uncertainty Quantification of a Low-Pressure Turbine Cascade by an Adaptive Gaussian Process. *Aerospace* **2023**, *10*, 1022. https://doi.org/10.3390/aerospace10121022

Academic Editor: Dries Verstraete

Received: 23 October 2023
Revised: 30 November 2023
Accepted: 6 December 2023
Published: 9 December 2023

Copyright: © 2023 by the authors. Licensee MDPI, Basel, Switzerland. This article is an open access article distributed under the terms and conditions of the Creative Commons Attribution (CC BY) license (https://creativecommons.org/licenses/by/4.0/).

1. Introduction

Affected by component mismatching and the variations of the flight environment, the inlet flow conditions of compressors and turbines often change in the real world. For different cruising altitudes, the inlet total pressure and Reynolds number of Low-Pressure Turbines (LPTs) fluctuate a lot. As flight attitude changes, flow distortion with varied total pressure and boundary layer can be commonly found at the inlet of the compressor. Under the influence of combustion instability, the inlet flow of a high-pressure turbine exhibits strong uncertainties, further exerting uncertainty impact on the downstream LPT [1,2]. In such situations, performance in service of the blades designed by deterministic methods, i.e., neglecting the effects of uncertainties, inevitably deviates from the design objective. Such design results in not only a decrease in mean performance but also in an increase in performance dispersion. To improve the mean performance and reduce the dispersion, robust design optimization has attracted wide attention. Ghisu et al. [3] found that the probability of compressor stall is considerable if considering the effects of stochastic inlet flow variations, especially under operation conditions with low rotational speed. They then performed robust design optimization by regarding the statistical performance as the objective and successfully decreased the probability of compressor stall. Luo et al. [4] found that the impact of stochastic variations of inlet flow angle on flow loss of a turbine cascade is severe under off-design operation conditions. They then performed robust design optimization and successfully improved the robustness by reducing the variance of flow loss. For robust design optimization, the evaluation of the uncertainty impact and calculation of the statistical performance is an issue. Usually, a large number of uncertainty quantifications are needed to conduct robust design optimization, which results in a great cost of computing resources. Therefore, the method of quantification is desired to be efficient and accurate at the same time.

With the development of computational fluid dynamics (CFD), more and more researchers have conducted uncertainty quantification (UQ) investigations of turbine cascades [5,6]. Different quantification methods have been developed [7], which are mainly divided into two categories, one based on sensitivity analysis and the other based on model methods. The sensitivity-based UQ analysis method is suitable for the case where nonlinear dependence between the output and input uncertainties is not strong. Putko et al. [8] used the method of moment (MM) to propagate the uncertainties of geometric changes and flow changes in quasi-one-dimensional flows. Luo et al. [9] and Xu et al. [10] evaluated performance changes using sensitivity-based UQ methods. Using this method, the computational cost for statistical analysis is significantly reduced. However, it cannot be used for strongly nonlinear uncertainty problems.

UQ methods based on surrogate models have been widely studied and applied. The polynomial chaos (PC) model is a popular method that constructs the model through the expansion of multiple sets of orthogonal random processes. Compared with Monte Carlo simulation (MCS), fewer samples are required by the PC method, while the prediction accuracy is high, making it more attractive [11]. Hosder et al. [12] applied the non-intrusive polynomial chaos (NIPC) method to a three-dimensional wing flow in which the stochastic variations of free flow Mach number and angle of attack are taken into account. Simon et al. [13] used a sparse PC method to study the transonic unsteady flow of airfoil under geometric uncertainty. Guo et al. [14] used the NIPC to evaluate the performance changes in a compressor cascade under the influence of installation angle and contour errors. Chen et al. [15] used the adaptive NIPC method to study the performance of a transonic compressor blade under the influence of uncertain inlet flow angle changes. Emory et al. [16] investigated the influence of the compounded variations of inlet total pressure, inlet turbulence intensity, and wall temperature on the performance changes in a turbine blade using NIPC. Moreover, Gopinathrao et al. [17] utilized the NIPC method to analyze the influence of stochastic variations of inlet total pressure on the changes in total pressure ratio and adiabatic efficiency of NASA Rotor 37. Tang et al. [18] constructed a Kriging model, which is a specific case of Gaussian process (GP) for performance prediction of a centrifugal compressor, in which the effects of stochastic variations of inlet flow angle, tip clearance, etc. are considered. In recent years, rapidly developed machine-learning methods have been widely used in various disciplines [19]. By machine learning, surrogate models can be constructed through supervised learning. Hu et al. [20] applied support vector regression to model construction, which was then used for predicting the aerodynamic performance of a transonic compressor. Wang et al. [21], He et al. [22], and Cao et al. [23] investigated the impact of uncertainties on performance changes in compressors using artificial neural networks (ANNs).

However, it is time-consuming for the training of ANN models that numerous hyperparameters, including the number of hidden layers and neurons on each hidden layer, etc., need to be optimized. By contrast, GP is more flexible without much fine-tuning of the hyperparameters due to its non-parametric features [24]. Additionally, GP exhibits higher accuracy compared to the NIPC method, which is also investigated in this study. Generally, it is necessary to construct a surrogate model with high response accuracy using as few training samples as possible. GP with adaptive sampling is a good choice. GP was originally developed as a probability theory concept by Wiener and Kolmogorov in the 1940s. It originated as a regression tool in geostatistics by Krige [25] and later found applications in spatial statistics [26], general regression [27], computer experiments [28], and machine learning [29]. In the context of machine learning, GP is applied in nonlinear regression and classification [29]. GP not only predicts the mean response of test points but also estimates the variance within the sampling space. This unique capability makes it easier to conduct adaptive sampling using the variance, resulting in a decrease in the number of training samples for model training. Due to these characteristics, GP has become popular in various applications [24,30].

From the aforementioned literature working on the performance impact of stochastic variations of inlet flow, the effects of inlet flow angle, inlet total pressure, and inlet turbulence intensity were considered in most cases. In the present study, uncertainty impact on the performance parameters, such as total pressure-loss, outflow angle, and Zweifel lift coefficient of an LPT cascade, will be investigated. It is well known that the changes in inlet flow angle and inlet total pressure should influence the lift of the turbine cascade, which subsequently changes the Zweifel lift coefficient and flow deviation at the outlet, while the change in inlet turbulence intensity usually has a strong impact on flow transition of LPT. Thus, the effects of inlet flow angle, inlet total pressure, and turbulence intensity are considered in the study; meanwhile, the adaptive Gaussian process (ADGP) is used for performance prediction. The organization of this paper is as follows. Flow simulations are first carried out, and the impacts of each uncertainty on performance changes are analyzed. The principles of ADGP are then introduced, and the method is verified and validated through a series of function experiments. The surrogate models of performance parameters with respect to the uncertainties are learned by ADGP. Using the models, performance changes in the LPT cascade are finally quantified. MCS-based statistical analysis of the flow fields is performed to reveal the impact mechanisms of uncertainties. Moreover, the results of the Sobol sensitivity analysis are given to illustrate the contribution of each uncertainty to performance changes.

2. Numerical Simulation

The two-dimensional cascade of the first rotor in a two-stage LPT of a small aero engine is utilized in the study. The uncertain effects of inlet flow angle α, inlet total pressure $P_{t,in}$, and inlet turbulence intensity Tu on the cascade flow are considered. The flow simulation adopts an in-house program, which solves the Reynolds-averaged Navier–Stokes (RANS) equations, SST turbulence model, and $\gamma - \widetilde{Re}_{\theta t}$ transition model equations. LU-SGS time-marching is used. Multigrid and local time step techniques are used to accelerate convergence.

In this paper, the total pressure-loss coefficient ζ, outlet flow angle β, and Zweifel number Zw of the turbine cascade are calculated. The total pressure-loss coefficient and Zweifel number are defined as:

$$\zeta = \frac{P_{t,in} - P_{t,out}}{P_{t,out} - P_{out}} \tag{1}$$

$$Zw = \frac{\int_0^1 (P_p - P_s) d(\frac{x}{c_x})}{P_{t,in} - P_{out}} \tag{2}$$

where P_t and P are total pressure and static pressure, respectively; the subscripts in and out represent inlet and outlet, respectively; the subscripts p and s represent pressure side and suction side, respectively; x and c_x are the distance from the leading edge and axial chord, respectively.

Specifications of the turbine cascade are given in Table 1, where the inlet total pressure $P_{t,in}$, inlet total temperature $T_{t,in}$, inlet flow angle α, turbulence intensity Tu and outlet back pressure P_{out} are given. The inlet total pressure and temperature are uniformly distributed in the circumferential direction, and a mass-averaged calculation is performed to obtain the outlet back pressure and angle. Figure 1 presents the cascade geometry and the topology of multi-block grids. Four sets of grids are used for flow simulations, the resolutions of which are 5×10^4, 6×10^4, 7.2×10^4, 8.6×10^4, respectively. Figure 2 shows the flow solutions of ζ, β, and Zw of the four different grids, where N is the serial number of the grids, w/w_4 is a scaled function representing the performance parameters, where the reference w_4 is the one for the fourth grid. It is evident that as the grid resolution increases, all the performance parameters approach those of the fourth grid. The results of the third and fourth grids are almost the same. The grid-independent flow solutions, including ζ, β, and Zw, are also given in Table 1. In the following study, the third grid is utilized.

Table 1. Specifications of the turbine cascade.

Parameter	Value
inlet total pressure $P_{t,in}$	294,679.4 Pa
inlet total temperature $T_{t,in}$	1238.9 K
inlet flow angle α	33.50°
inlet turbulence intensity Tu	0.025
outlet static pressure P_{out}	201,017 Pa
axial chord c_x	0.0165 m
total pressure-loss coefficient ζ	0.0317
outlet flow angle β	−61.20°
Zweifel number Zw	0.8682

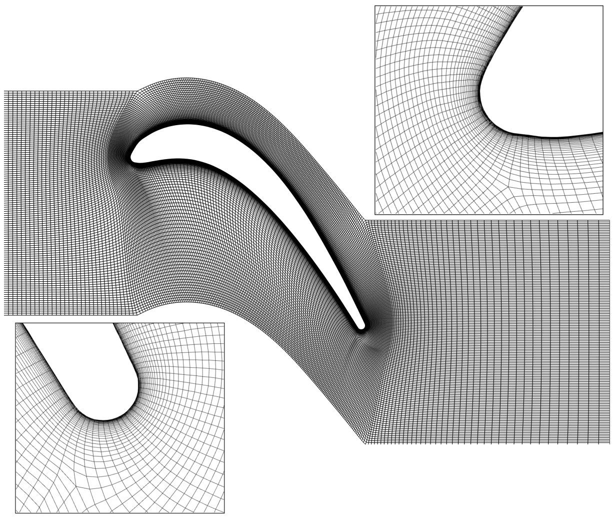

Figure 1. Mesh of the cascade.

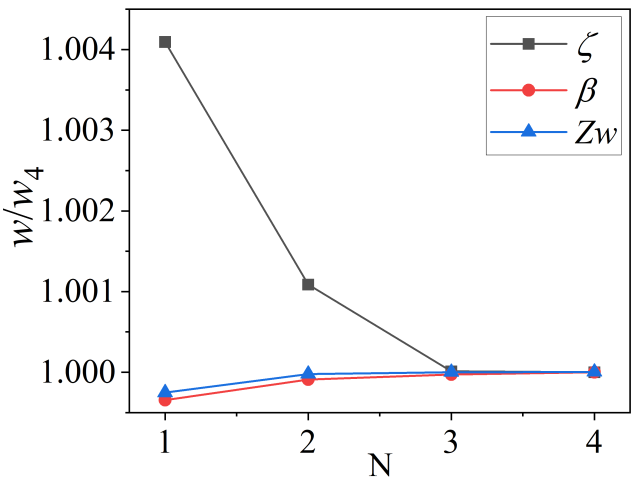

Figure 2. Grid-independent flow solutions.

To demonstrate the effects of inlet flow parameters on the aerodynamic performance changes, inlet total pressure $P_{t,in}$ and inlet flow angle α are perturbed in the interval

$[-10\%, 10\%]$, while the turbulence intensity Tu is perturbed in the interval $[-60\%, 60\%]$. The relative variations of the inlet flow parameters are defined as

$$\Delta f = \frac{f - f_{ref}}{f_{ref}} \tag{3}$$

where f is a universal function representing $P_{t,in}$, α, and Tu, and the subscript ref denotes the reference value. Figure 3 presents the relative variations of performance parameters versus the relative variations of inlet flow parameters. Generally, the impact of inlet flow variations on the changes in ζ are considerable. At the interval boundaries, more than 2% variations in ζ can be found. It is obvious that the increase of inlet flow angle and turbulence intensity induce more flow losses to the turbine cascade, while the increase of inlet total pressure is effective in reducing the flow loss. By contrast, the impact of inlet flow parameters on outlet flow angle is rather weak since the maximum relative variation of β is about 0.4%. Moreover, β is almost independent of the variations of inlet flow angle and turbulence intensity. Similar results can be found for the variations of the Zweifel number, as shown in Figure 3c. Besides the inlet total pressure, the inlet flow angle also changes Zweifel number obviously. It is known that both outlet flow angle and Zweifel number are closely dependent on the lift of the turbine cascade. The increase of inlet flow angle and inlet total pressure has been well recognized to be effective in increasing blade loading, which undoubtedly results in increased Zweifel number and increased flow-turning angle. It should be noticed that in Figure 3b, as $\Delta\alpha$ increases, the negative relative change in outlet flow angle is attributed to the increased inlet flow angle, although the flow-turning angle increases. Moreover, as shown in Figure 3c, the decrease of Zweifel number resulting from inlet total pressure increase is attributed to the increase of $P_{t,in}$, as shown in Equation (2).

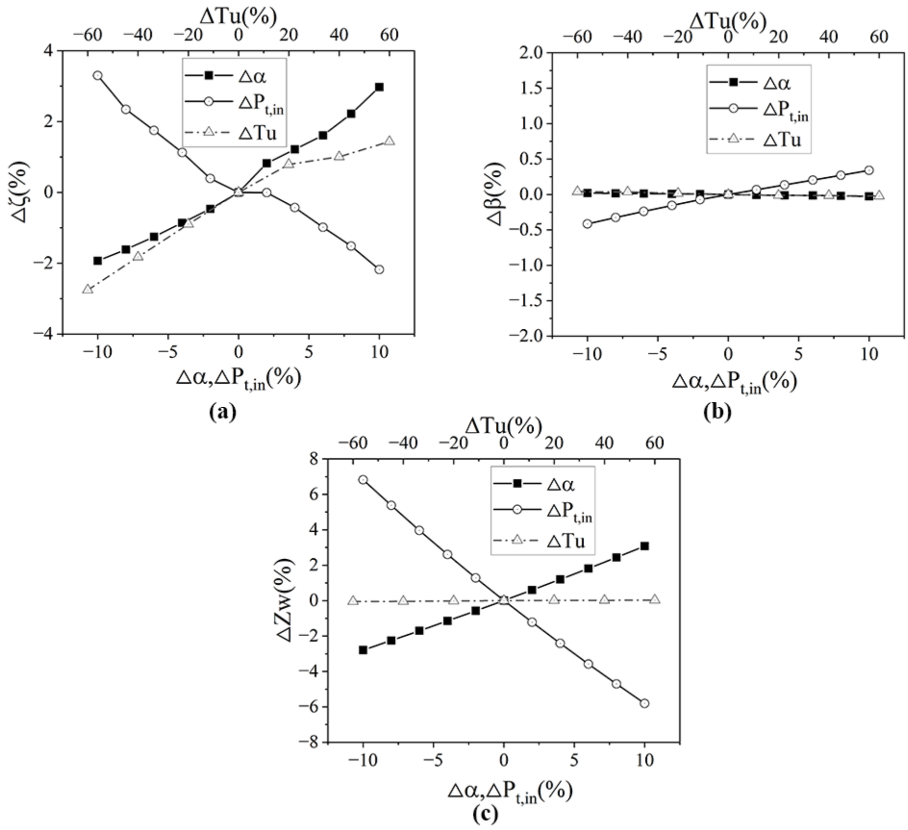

Figure 3. Performance parameter changes versus inlet flow parameter variations: (**a**) $\Delta\zeta$; (**b**) $\Delta\beta$; (**c**) ΔZw.

It is well known that the occurrence of laminar flow transition on the suction side of the turbine cascade can usually be found, which immediately and significantly changes the flow loss. To further understand the impact mechanisms of inlet flow variations on the changes of total pressure-loss coefficient, the contours of intermittency factor in the boundary layer of the suction side of the turbine cascade are given in Figure 4. Figure 4b–d are the contours with maximum absolute variations of inlet flow angle, inlet total pressure, and turbulence intensity, respectively. From Figure 4b,d it can be observed that when $\Delta\alpha$ and ΔTu are 10% and 60%, respectively, flow transition on the suction side moves upstream compared with the contour as shown in Figure 4a. When $\Delta\alpha$ and ΔTu are -10% and -60%, respectively, flow transition on the suction side moves downstream, resulting in reduced flow losses. However, as shown in Figure 4c, the movements of flow transition on the suction side under varied inlet total pressure are opposite compared with those given in Figure 4b,d. In such situations, $\Delta\zeta$ with respect to $\Delta P_{t,in}$ exhibits totally different variations compared with those with respect to $\Delta\alpha$ and ΔTu, as shown in Figure 3a.

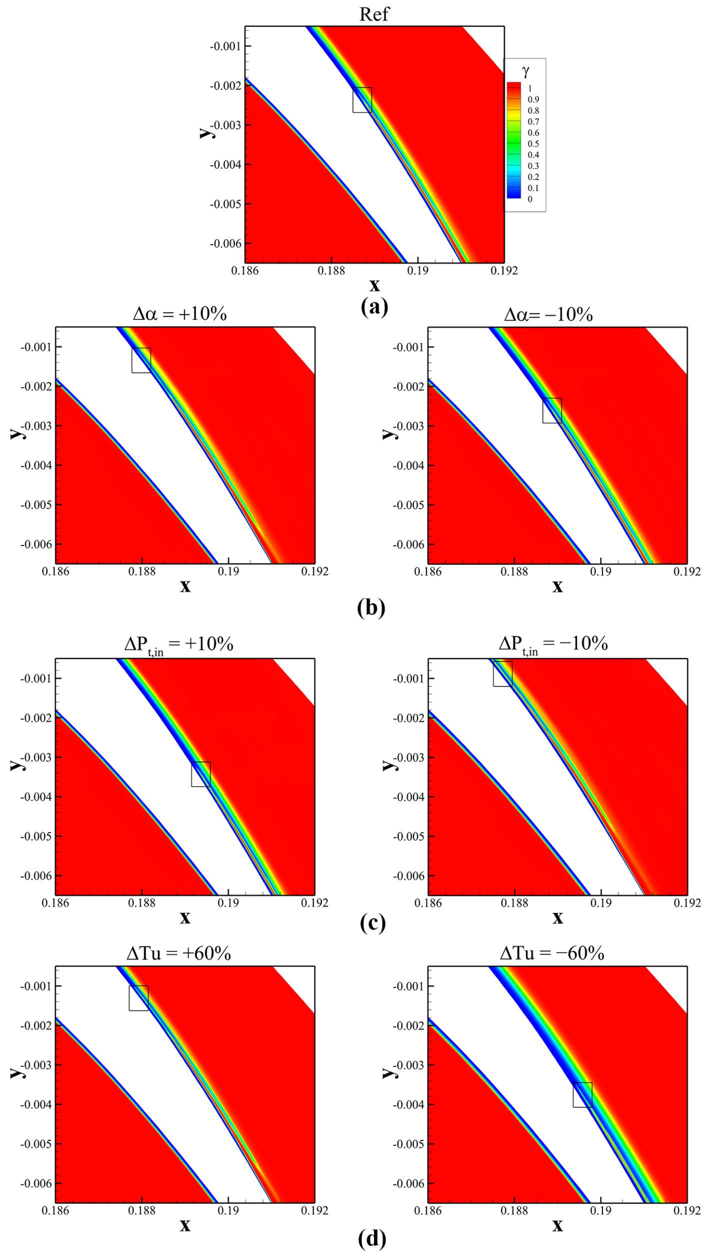

Figure 4. Contours of intermittency factor: (**a**) Ref; (**b**) $\Delta\alpha$; (**c**) $\Delta P_{t,in}$; (**d**) ΔTu.

3. Adaptive Gaussian Process

3.1. Gaussian Process

In probabilistic statistical theory, GP is an important branch of the stochastic process, which is defined as a Gaussian process, which is a collection of random variables, any finite number of which have a joint Gaussian distribution [29]. From the perspective of function space, GP can be described succinctly. GP is completely specified by its mean function and covariance function. The mean function $m(x)$ and the covariance function $k(x, x')$ for a real-valued Gaussian process $f(x)$ are defined as follows:

$$m(x) = E[f(x)] \tag{4}$$

$$k(x, x') = E[(f(x) - m(x))(f(x') - m(x'))] \tag{5}$$

GP $f(x)$ can be written as:

$$f(x) \sim GP(m(x), k(x, x')) \tag{6}$$

Usually, for notational simplicity, the mean function is assumed to be zero, although this does not need to be done. The random variable in the definition represents the function value $f(x)$. x can be either time or a multidimensional parameter.

Covariance functions are also called kernel functions, which define nearness or similarity between data points. There are many choices for specifying the kernel functions, such as squared exponential functions, quadratic rational functions, Matern-class functions, etc. In the present study, the squared exponential function is used as the kernel function:

$$k(x^p, x^q) = \sigma_\alpha \exp\left(-\sum_{l=1}^{n} \frac{(x_l^p - x_l^q)^2}{2\sigma_l^2}\right) \tag{7}$$

where σ_α is the output length scale, x_l is the l-th component of the input vector, σ_l is the feature-length scale on the dimension l. Given a training set (X, Y), where X is the set of input variables, and Y is the set of corresponding output values, the output values at the test points X_* satisfy the following joint Gaussian distribution:

$$\begin{bmatrix} Y \\ f^* \end{bmatrix} \sim N(0, \begin{bmatrix} K(X,X) + \sigma_n^2 & K(X, X_*) \\ K(X_*, X) & K(X_*, X_*) \end{bmatrix}) \tag{8}$$

where σ_n^2 is the observed noise variance. Then the conditional distribution of f_* can be determined as:

$$f_*|X, Y, X_* \sim N(\overline{f_*}, cov(f_*)) \tag{9}$$

$$\overline{f_*} = K(X_*, X)[K(X,X) + \sigma_n^2 I]^{-1} Y \tag{10}$$

$$cov(f_*) = K(X_*, X_*) - K(X_*, X)[K(X,X) + \sigma_n^2 I]^{-1} K(X, X_*) \tag{11}$$

The hyperparameters σ_n^2, σ_l^2 and σ_α can be determined by maximizing the marginal likelihood function. The expression of the marginal likelihood function is given by Equation (11), where $K(X, X)$ is simplified to K:

$$logp(Y|X) = -\frac{1}{2} Y^T (K + \sigma_n^2 I)^{-1} - \frac{1}{2} log|K + \sigma_n^2 I| - \frac{n}{2} log 2\pi \tag{12}$$

Fitting the optimal value of the hyperparameters is essentially one kind of optimization problem, which can be quickly achieved using the ADAM gradient-based method [31].

3.2. Adaptive Sampling

The accuracy of the GP regression model depends largely on the selection of training samples. Training samples can be selected by manual one-time selection (such as random or uniform sampling in the sample space) or adaptive sampling. The GP regression model can predict the mean and variance of any test point in the sampling space. The variance represents the uncertainty of output, which can be used for adaptive sampling.

In the iterative sampling process, the ADGP determines the new required training samples according to the position of the maximum uncertainty. The new training samples are further included in the training set. The hyperparameter optimization is carried out in each interaction. In such a way, the accuracy of the model will be improved step by step, which is more scientific and efficient than manual one-time selection.

The standard ADGP usually produces only one sample per iteration. To improve sampling efficiency, this paper adopts the batch sampling method, which can add multiple samples per iteration. The GP based on batch sampling also has a disadvantage, i.e., the newly sampled points may be clustered within a certain range. To avoid this situation, after obtaining the first newly sampled point with the largest uncertainty in each iteration, the covariance matrix of GP is updated using the renewed samples directly without retraining the model, and then sampling for selecting the second new sample point [32].

The key point of adaptive sampling is the sampling criterion. In the study, the standard deviation predicted by the model is used as the acquisition function to guide the sampling. A convergence threshold is given to stop the adaptive sampling. The acquisition function is as follows:

$$f_{acq}(x) = \sigma(x) \tag{13}$$

Figure 5 gives the flowchart of ADGP. The processes can be briefly described as follows.

Step 1: The initial training sets are prepared for GP training, and a batch of test sets are prepared for prediction.

Step 2: Train the GP model by hyperparameter optimization, which is then used for function predictions of the test sets.

Step 3: Calculate the acquisition function f_{acq} at each test point and determine the maximum $f_{acq,max}$, which is then compared with the threshold.

Step 4: If $f_{acq,max} \leq \epsilon$, model training can be completed, where ϵ is the threshold. If $f_{acq,max} > \epsilon$, the current GP model does not meet the accuracy requirement. The first selected test point is added to the training sets. Calculate the f_{acq} for the second time and determine the maximum $f_{acq,max}$, which is then compared with the threshold.

Step 5: If $f_{acq,max} \leq \epsilon$, model training can be completed. If $f_{acq,max} > \epsilon$, the second selected test point is added to the training sets and goes to **Step 2**.

It should be noted that after adding the first selected test point to the training sets, it is not necessary to train the GP model following **Step 2**, while only the covariance matrix needs to be updated. In this way, two new training samples can be selected per each iteration.

3.3. Function Test

To verify the prediction accuracy of ADGP and the computational cost of model training, three different function experiments are presented. Moreover, GP without adaptive sampling and the widely used adaptive NIPC method are also used, and the results are compared. The functions are given as follows.

Himmelblau function (2-d) [33]:

$$f(\boldsymbol{x}) = (x_1^2 + x_2 - 11)^2 + (x_2^2 + x_1 - 7)^2, \;\; x_1, x_2 \in [-3,\; 3] \tag{14}$$

Four-dimension function (4-d) [34]:

$$f(\boldsymbol{x}) = \frac{2}{3}e^{x_1+x_2} - x_4\sin(x_3) + x_3, \quad x_1, x_2, x_3, x_4 \in [0,\ 1] \tag{15}$$

Six-dimension function (6-d):

$$f(\boldsymbol{x}) = 0.05 * (\sum_{i=1}^{6}(x_i + x_i^2 + x_i^3 + x_i^4) + \sum_{i=1}^{5}\sum_{j=i+1}^{6} x_i x_j) + 0.5 \tag{16}$$

where $\boldsymbol{x} = (x_1, x_2, x_3, x_4, x_5, x_6)$ and $x_i \in [-1,1]$, $i = 1, \cdots, 6$.

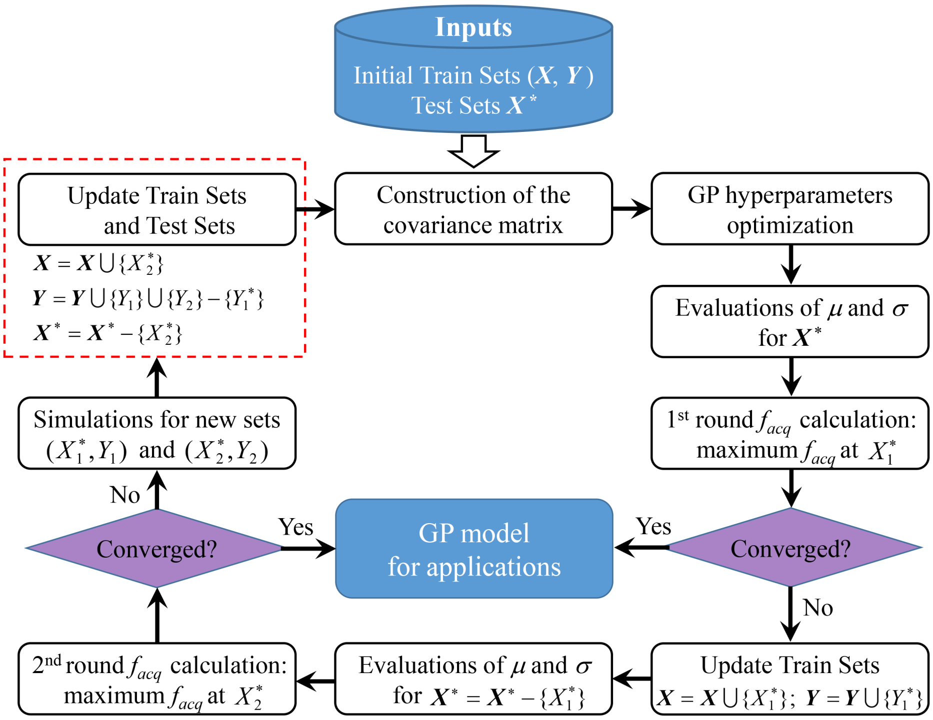

Figure 5. Procedures of adaptive Gaussian process.

In the domain of function definition, initial training samples of ADGP are obtained by the Latin Hypercube Sampling (LHS) method. The numbers of initial training samples and the thresholds for the three function experiments are given in Table 2, where n_0 and n_t are the numbers of initial and total training samples, respectively. Figure 6 presents the convergence history of the maximum acquisition function $f_{acq,max}$, where N means the iteration counter. Starting from the initial training samples, $f_{acq,max}$ decreases, demonstrating the exploitation phase of adaptive sampling and that the prediction accuracy of ADGP is gradually improved.

Table 2. Parameters of the function experiments.

	n_0	ϵ	n_t
2-d	6	0.02	36
4-d	12	0.05	66
6-d	16	0.15	66

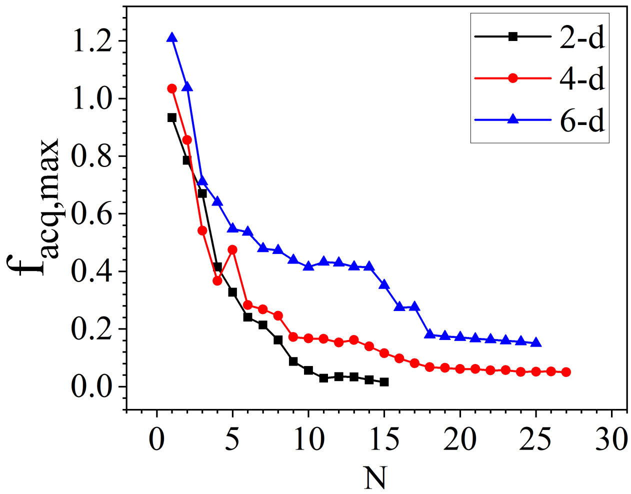

Figure 6. Convergence history of the maximum acquisition function.

To compare the prediction accuracy of different surrogate models, for each function experiment, the same number of training samples are generated by LHS for static GP and adaptive NIPC. The principles and procedures of an adaptive NIPC based on a sparse grid sampling technique have already been introduced in previous studies [15,35]. In the study, after trying polynomials of different orders, seven-order polynomials are used, and the numbers of total samples are maintained with those of ADGP. Moreover, a large number of points are selected in the function domain and used as the test samples for assessing the prediction accuracy of surrogate models. The prediction accuracy is measured by mean absolute percentage error (MAPE), the definition of which is given as

$$\mathrm{MAPE} = \frac{1}{n}\sum_{i=1}^{n}\left|\frac{f_{i,model} - f_{i,exact}}{f_{i,exact}}\right| \times 100\% \tag{17}$$

where f_i is the prediction of i-th sample, n is the number of test samples, the subscripts *model* and *exact* represent model prediction and exact values, respectively.

Table 3 shows the MAPE of the three models, where GP and ANIPC are static GP and adaptive NIPC, respectively. It is obvious that compared with static GP and ANIPC, the prediction accuracy of ADGP is higher in all three function experiments using the same number of training samples. Moreover, the prediction accuracy of both static GP and ADGP is higher than that of ANIPC, demonstrating that machine learning is useful in improving the prediction accuracy of the surrogate models.

Table 3. MAPE of different function experiments by the surrogate models.

	2-d	**4-d**	**6-d**
GP	10.594	8.873	4.933
ADGP	1.764	4.248	3.760
ANIPC	216.7	683.2	194.2

To better distinguish the difference of sample distributions in the same function domain, Figure 7 shows the original two-dimensional function and the distributions of training samples. Compared with the sample distribution of both static GP and ADGP, the samples of adaptive NIPC are concentrated in the adjacent region of maximum value. That is because the new sparse grids are produced by a simple interpolation method, and more grids are required to reduce the interpolation error near the maximum value. In Figure 7d, the red and black points are the initial and adaptively generated training samples, respectively. Compared with the agglomerative sample distribution of adaptive NIPC, the samples of ADGP are more uniformly distributed on the boundaries.

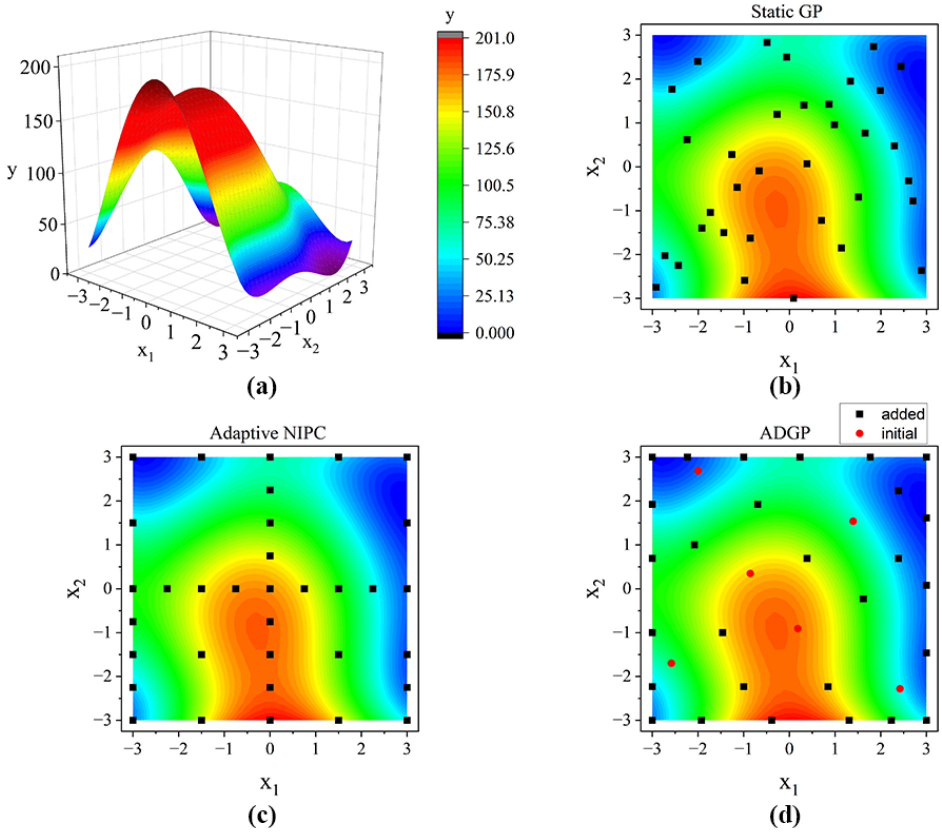

Figure 7. Sample distributions of the 2-d function experiments: (**a**) function; (**b**) static GP; (**c**) adaptive NIPC; (**d**) ADGP.

3.4. ADGP for Aerodynamic Parameters

In the following, ADGP will be used for predicting the aerodynamic performance of the turbine cascade, as shown in Figure 1. The compounded effects of inlet flow angle, inlet total pressure, and turbulence intensity are taken into account. For each performance parameter of total pressure-loss coefficient ζ, outflow angle β, and Zweifel number Zw, the corresponding surrogate model based on ADGP will be trained. Following the same procedures as shown in Figure 5, eight initial training samples are used. The threshold of the acquisition function is 0.1 for ζ and β, while it is 0.01 for Zw. Notice that all the training samples are generated in the same space as mentioned before, i.e., the uncertainty is 10% for inlet total pressure and inlet flow angle, and it is 60% for inlet turbulence intensity.

Figure 8 shows the convergence histories of $f_{acq,max}$ for the three performance parameters. After 10, 4, and 3 iterations, the maximum acquisition function of ζ, β and Zw, respectively, decreases to below the corresponding threshold. The total sample numbers are 28, 16, and 14 for training the ADGP models of ζ, β and Zw, respectively. The samples necessary for training the ADGP models of β and Zw are much less than those of ζ. It is mainly attributed to the more weakened nonlinear dependence of β and Zw on the inlet flow variations, as shown in Figure 3b,c. As shown in Figure 3a, ζ is nonlinearly dependent on the inlet flow variations. It thus requires more training samples for model training.

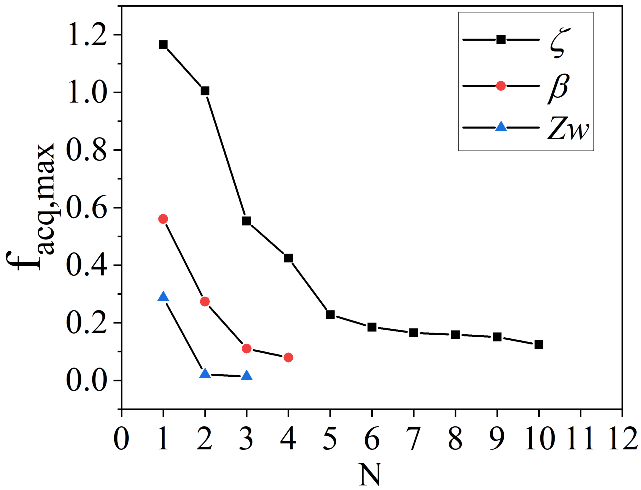

Figure 8. Convergence history of the maximum acquisition function.

Again, the prediction accuracy of the ADGPs is evaluated by several test samples. Four thousand test samples agreeing with the following Gaussian distribution are generated, which will also be used in the following UQ studies.

$$f(\xi) = \begin{cases} \frac{1}{\sqrt{2\pi}} \exp(-\frac{\xi^2}{2}), \xi \in [-E, E] \\ 0, otherwise \end{cases} \tag{18}$$

where E is the truncation boundary and $E = 2.0$ in the study, ξ is the scaled uncertainty variable satisfying the normal Gaussian distribution with the definition:

$$\xi = \frac{x - x_{ref}}{\sigma_x} \tag{19}$$

where x is the universal uncertainty variable considered in the study (inlet flow angle, inlet total pressure, inlet turbulence intensity), x_{ref} is the reference value under the baseline operation condition, which equals the statistical mean of x, σ_x represents the standard deviation of uncertainty variable x. In the present study, the standard deviations are 5, 5, and 30 for the relative variations of inlet flow angle, inlet total pressure, and inlet turbulence intensity, respectively. In such situations, the maximum relative variations of inlet flow angle, inlet total pressure, and inlet turbulence intensity are 10%, 10%, and 60%, respectively.

Performance parameters of each test sample are predicted by the corresponding ADGP. Then MAPE is calculated and shown in Table 4. The prediction accuracy of all ADGPs is high enough, and they can be used in the following UQ studies.

Table 4. MAPE of performance prediction by ADGP.

Parameter	MAPE(%)
ζ	0.2420
β	0.0062
Zw	0.0089

4. Results and Discussion

4.1. Uncertainty Quantification and Statistical Analysis

Due to the limitations of long-term experimental measurement, no exact distribution can be found so far to describe the inlet flow variations in the real world. In this study, the inlet flow variations of the turbine cascade are assumed to meet the Gaussian distribution, as shown by Equation (18).

Before assessing the performance changes due to inlet flow variations using ADGPs, statistical analysis using MCS is conducted, by which the exact statistical mean and standard deviation can be obtained. The group of 4000 test samples used for calculating MAPE, as shown in Table 4, is used in the present MCS-based statistical analysis. Figure 9 shows the convergence history of MCS-based statistics including the mean μ and standard deviation σ of ζ, β and Zw. When the number of test samples exceeds 3000, the statistics remain almost unchanged. The converged statistics obtained by MCS will be regarded as the exact ones in the following study.

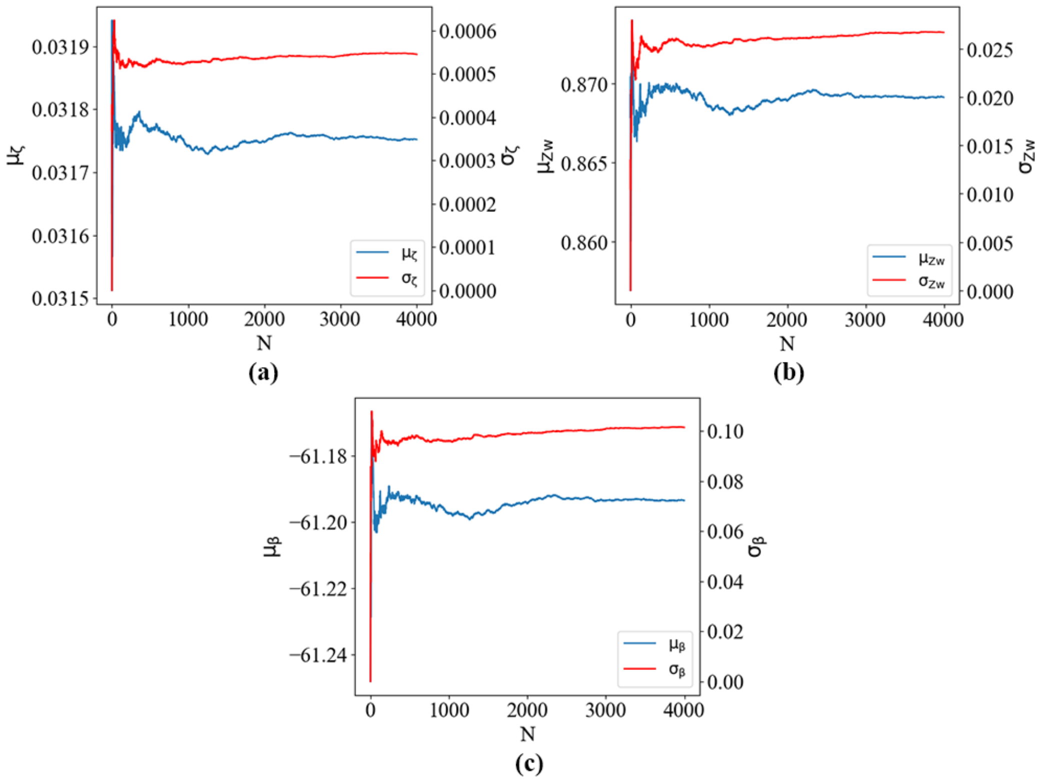

Figure 9. Convergence history of MCS-based statistics: (**a**) ζ; (**b**) β; (**c**) Zw.

Using the ADGPs trained by the samples as shown in Figure 8, the performance parameters of all the four thousand test samples can be rapidly calculated, and the statistical mean and standard deviation of ζ, β and Zw can be subsequently determined. Table 5 gives the statistics $\mu_{\Delta f}$ and $\sigma_{\Delta f}$ of performance changes, where Δf represents the relative variation of performance parameter. Meanwhile, the relative deviations between the ADGP-based statistics and the MCS-based ones, ε_μ and ε_σ, are also calculated and given in the table. The relative deviations of all statistics are small, demonstrating satisfied prediction accuracy of ADGPs for the quantifications of performance changes in the turbine cascade. Moreover, it can be concluded that the outflow angle is rather insensitive to inlet flow variations because the statistical mean and standard deviation of outflow angle change are almost zero. The total pressure-loss coefficient and Zweifel number are comparatively more sensitive to inlet flow variations. As we know, the standard deviation is widely used to evaluate the dispersion of performance parameters. From the results, it can be known that the Zweifel number is the most dispersive, while the outlet flow angle is the most assembled.

Table 5. Statistics obtained by ADGP and the relative deviation from the MCS results.

Parameter	$\mu_{\Delta f}(\%)$	$\sigma_{\Delta f}(\%)$	$\varepsilon_{\mu}(\%)$	$\varepsilon_{\sigma}(\%)$
ζ	4.943×10^{-2}	1.759	-3.797×10^{-2}	2.403
β	-4.656×10^{-3}	0.162	7.602×10^{-4}	-2.231
Zw	1.112×10^{-1}	3.080	3.747×10^{-4}	0.178

Figure 10 gives the probability density function (PDF) of performance parameters determined from the four thousand test samples. Meanwhile, the Gaussian distributions with the same statistical mean and standard deviation are also given in the figures. From the distributions, it can be observed that the PDFs of $\Delta\zeta$ and $\Delta\beta$ obtained by ADGP are slightly left skewed, demonstrating weak nonlinear dependence of total pressure-loss coefficient and outlet flow angle on inlet flow variations. By contrast, the PDF of ΔZw obtained by ADGP is close to the Gaussian distribution, demonstrating that the Zweifel number is almost linearly dependent on inlet flow variations. In fact, the linear dependence of Zweifel number on inlet flow parameters can also be found in Figure 3c, where Zw exhibits linear variations in the variation ranges of inlet flow angle, inlet total pressure, and turbulence intensity.

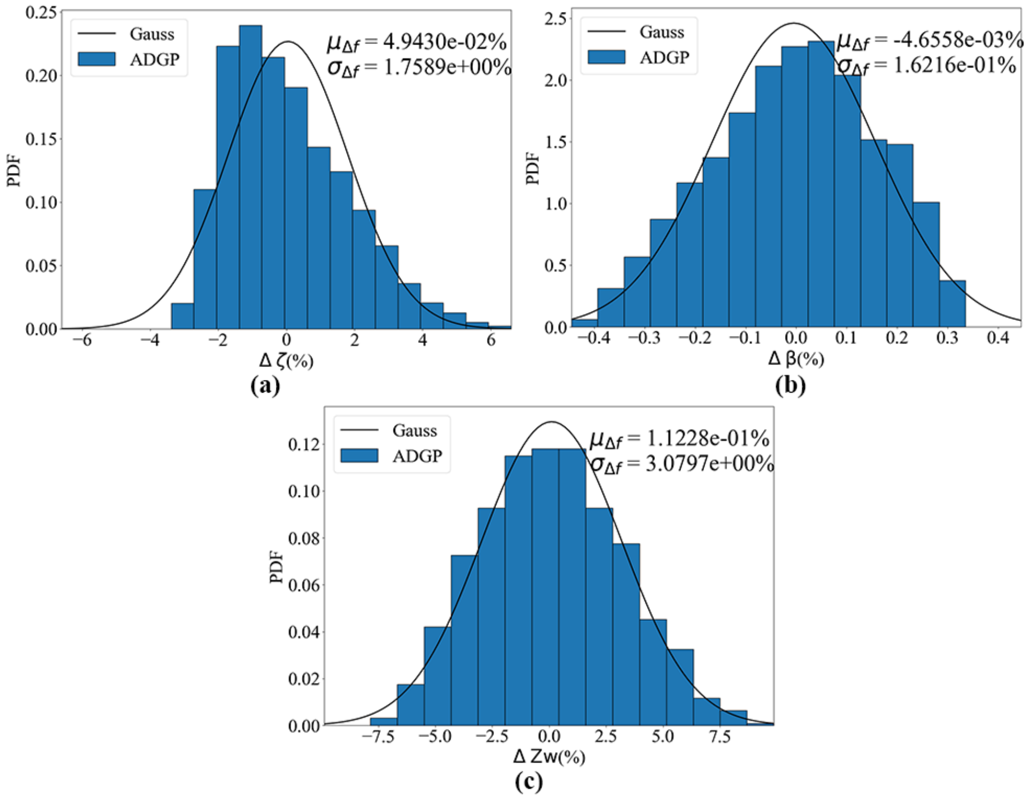

Figure 10. PDF distributions of: (**a**) ζ; (**b**) β; (**c**) Zw.

Statistical analysis of the flow field has been proven to be able to further uncover the sources of uncertainty performance impact and the impact mechanisms [36,37]. In the study, the flow fields of the four thousand test samples are collected, based on which the means and standard deviations of all the interested flow variables of the turbine cascade can be obtained. Most of the time, the statistics of the relative variations of flow variables compared to the flow field under the reference flow conditions are useful to uncover the impact mechanisms.

From the results shown in Figure 4, it can be observed that flow transition on the suction side of the turbine cascade is sensitive to the inlet flow variations, which is quite possibly the main source of the uncertain variations of flow losses. Figure 11 illustrates the contours of the statistical mean and standard deviation of the relative variation of intermittency factor $\Delta\gamma$, the definition of which is:

$$\Delta\gamma = \frac{\gamma - \gamma_{ref}}{\gamma_{ref} + \delta} \times 100\% \tag{20}$$

where δ is a tiny number, and the subscript ref denotes the reference value. The figures clearly show that the suction flow transition is indeed the most sensitive to inlet flow variations because the standard deviation near the wall of the suction side is much higher, as shown in Figure 11b. Moreover, as shown in Figure 4a, flow transition occurs at the position downstream $x = 0.188(x/c_x = 0.73)$. Figure 11a shows that the mean flow transition slightly moves upstream when considering uncertainty impact, which results in the increase of flow losses.

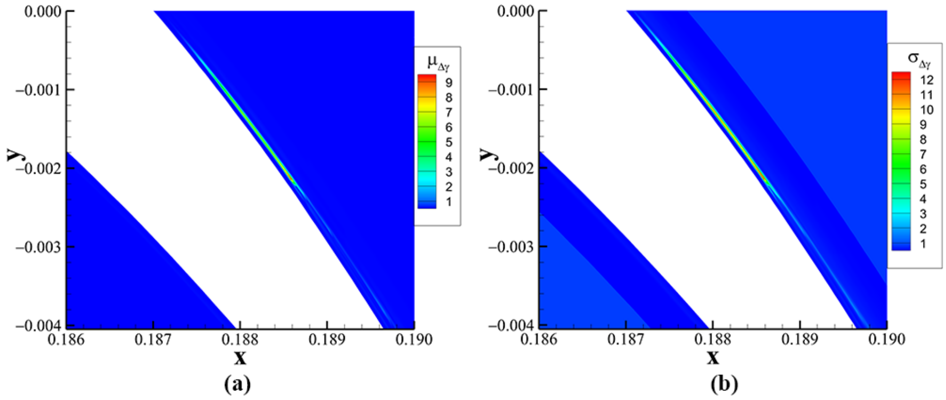

Figure 11. Contours of the statistics of relative variation of intermittency factor: (**a**) mean; (**b**) standard deviation.

To further uncover the impact mechanisms, the variations of flow solutions on the suction side of the turbine cascade are given in Figure 12. This figure gives the distributions of statistical mean and standard deviation of the relative variation of viscous shear stress $\Delta\tau$, the definition of which is:

$$\Delta\tau = \frac{\tau - \tau_{ref}}{\tau_{ref} + \delta} \times 100\% \tag{21}$$

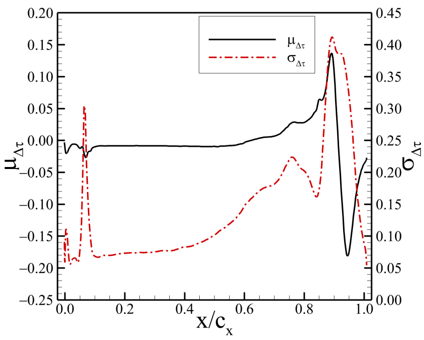

Figure 12. Distributions on the suction side of the statistics of the relative variation of viscous shear stress.

Because of the variation of inlet angle, the cascade meets the strike from a different direction of the flow, which obviously influences the flow acceleration at the leading edge and results in a small peak of the statistics of $\Delta\tau$ near the leading edge. It can be found that on the suction side, the statistics of $\Delta\tau$ rapidly increase on the portions downstream $x/c_x = 0.6\,(x = 0.186)$ and reach the peaks at about $x/c_x = 0.9\,(x = 0.191)$. The results shown in Figures 11 and 12 demonstrate that the inlet flow variations have a strong impact on the variations of flow transition and, thus, viscous shear stress.

4.2. Sobol Sensitivity Analysis

In the above UQ studies, the compounded influence of three different inlet flow parameters is considered. To distinguish the influence of each inlet flow parameter on performance changes in the turbine cascade, Sobol sensitivity analysis [38] is carried out. The principle of Sobol sensitivity analysis is briefly introduced in the following.

Suppose Y is a scalar output depending on the input $\boldsymbol{x} = (x_1, x_2, \cdots, x_{n_d})$.

$$Y = f(x_1, x_2, \cdots, x_{n_d}) \tag{22}$$

where n_d is the dimensionality of the input. By calculating $V_{x_i}(E_{\boldsymbol{x}_{\sim i}}(Y|x_i))$, we can obtain the first-order effect about x_i, where $\boldsymbol{x}_{\sim i}$ means the input vector without the i-th component and V means the variance. Correspondingly, the first-order sensitivity index of x_i is:

$$S_i = \frac{V_{x_i}(E_{\boldsymbol{x}_{\sim i}}(Y|x_i))}{V(Y)} \tag{23}$$

The total sensitivity index of x_i consists of the sum of the first and higher order sensitivities about x_i. In addition, the coupled effects of two components, x_i and x_j, can be evaluated using a second-order sensitivity index.

$$S_{ij} = \frac{1}{V(Y)}\left[V_{x_i x_j}(E_{\boldsymbol{x}_{\sim ij}}(Y|x_i, x_j)) - V_{x_i}(E_{\boldsymbol{x}_{\sim i}}(Y|x_i)) - V_{x_j}(E_{\boldsymbol{x}_{\sim j}}(Y|x_j))\right] \tag{24}$$

The sensitivities satisfy the following relationships:

$$S_{T_i} = S_i + \sum_{j \neq i}^{n_d} S_{ij} + \cdots + S_{1,2,i,\ldots,n_d} \tag{25}$$

$$\sum_{i=1}^{n_d} S_i + \sum_{i<j}^{n_d} S_{ij} + \cdots + S_{12\ldots n_d} = 1 \tag{26}$$

Figure 13 shows the total sensitivities (STs) of performance parameters to each inlet flow parameter. For the total pressure-loss coefficient, the contributions of the three inlet flow parameters to performance change are similar, indicating that the performance impact of each inlet flow parameter needs to be considered. For the outflow angle, the total sensitivity to inlet total pressure is close to 1.0, indicating that the variation of inlet total pressure plays a dominant role in influencing the outflow angle. In Figure 13c, similar results can be found for the Zweifel number. The variation of Zw is dominantly attributed to the inlet total pressure variation. Moreover, the impact of the inlet flow angle on Zw variation also needs to be considered.

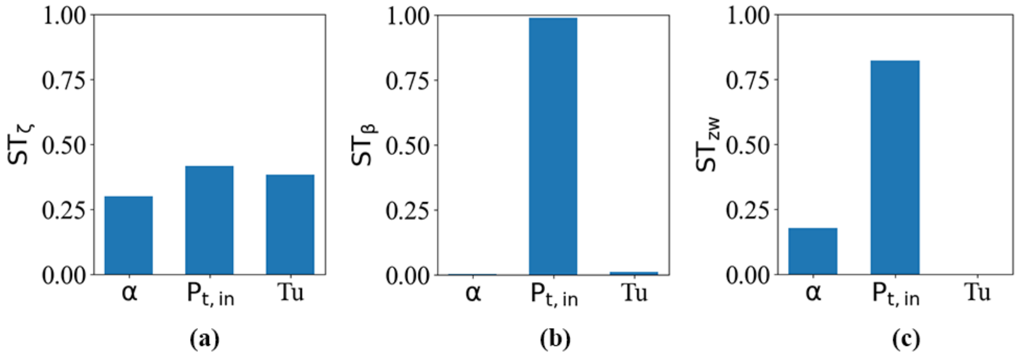

Figure 13. Total sensitivity index: (**a**) ζ; (**b**) β; (**c**) Zw.

Further understanding of the approximately equivalent impact of inlet flow angle, inlet total pressure, and inlet turbulence intensity on the variations of ζ can be found in Figure 3a. In the relative variation range of each inlet flow parameter, ζ exhibits evident monotonic variation. Considering the impact of inlet flow angle and inlet total pressure, the absolute maximum relative change in ζ is about 3.5%, while it is about 3% considering the effects of inlet turbulence intensity. These results illustrate that the contributions of the three inlet flow parameters to the variations of ζ are almost the same. To better understand the discrepant STs as shown in Figure 13b,c, Figure 14 presents the pressure distributions on the blade. It is the most distinct that even considering the effects of maximum relative variations of inlet turbulence intensity, i.e., $\Delta Tu = \pm 60\%$, the pressure distributions are almost duplicates of those under the reference condition, indicating that, under the inlet turbulence intensity variation, it is hard to significantly change the outflow angle and Zweifel number. That is why the STs of β and Zw with respect to Tu are almost zero. Moreover, in the case of $\Delta P_{t,in} = +10\%$, the loading is significantly higher than that under the reference condition, while it is significantly lower in the case of $\Delta P_{t,in} = -10\%$. The results demonstrate that the inlet total pressure variation can significantly change the outflow angle and Zweifel number. That is why the STs of β and Zw with respect to $P_{t,in}$ are the largest. Moreover, Figure 14a illustrates the moderate influence of inlet flow angle variation on loading change, from which it is known that the ST of Zw with respect to α is also moderate, as shown in Figure 13c. However, the ST of β with respect to α is almost zero, which requires further investigation.

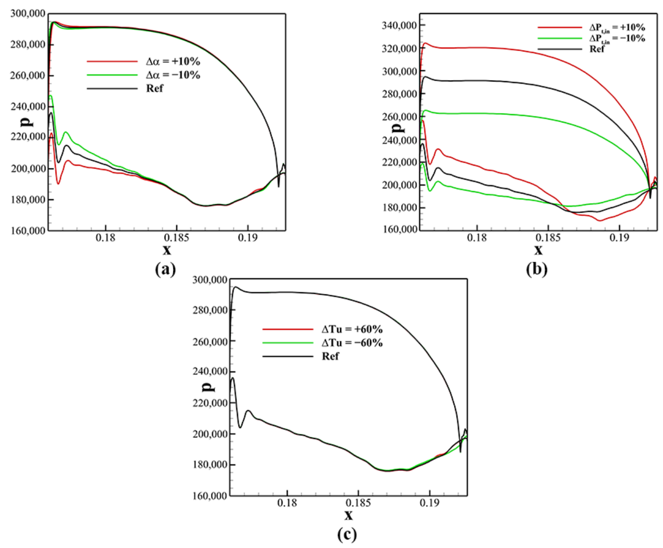

Figure 14. Pressure distributions on the blade considering the effects of: (**a**) α; (**b**) $P_{t,in}$; (**c**) Tu.

Figure 15 shows the second-order sensitivities (S2s) of performance parameters to pairwise inlet flow parameters, such as α-$P_{t,in}$, α-Tu, $P_{t,in}$-Tu. From Figure 15a,b, it is known that the coupled effects of $P_{t,in}$-Tu on total pressure-loss coefficient and outlet flow turning are strong, although Tu alone has almost no impact on outlet flow turning. The results demonstrate that when the impact of inlet total pressure and turbulence intensity are considered simultaneously, the variation of outlet flow angle is considerable. Moreover, although $P_{t,in}$ alone has a strong impact on outlet flow angle and Zweifel number, the coupled effects of α-$P_{t,in}$ on the variations of outlet flow angle and Zw are weak. Furthermore, the coupled effects of $P_{t,in}$-Tu on the variation of Zw are almost invisible.

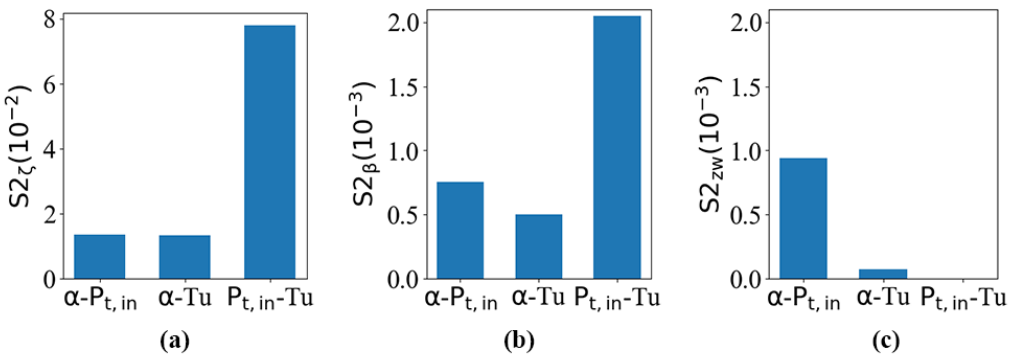

Figure 15. Second-order sensitivity index: (**a**) ζ; (**b**) β; (**c**) Zw.

5. Conclusions

The paper investigates the performance impact of uncertain inlet flow variations of an LPT cascade using an adaptive Gaussian process. First, flow simulations of the LPT cascade are conducted by solving the RANS equations, SST turbulence model, and transition equations. Through a careful grid-independent study, the converged flow solutions and the grid are specified. Then, the principles of the ADGP are introduced, and the prediction performance is verified and validated. These methods are used in the uncertainty impact study. The main conclusions are as follows:

(1) By comparing the methods of adaptive NIPC and GP with static sampling, the prediction accuracy of ADGP introduced in the study is proved to be higher through a function experiment. The machine-learning-based model training can find the optimal hyperparameters. The ADGP is then further verified and validated by accurately predicting the performance parameters of an LPT cascade.

(2) For this LPT cascade, the total pressure-loss coefficient and Zweifel number are sensitive to the uncertain variations of inlet flow parameters, while the outlet flow angle is almost insensitive to the uncertainties. Statistical analysis of the flow field demonstrates that flow transition on the suction side of the LPT cascade and the viscous shear stress are rather sensitive to uncertainties, which can be regarded as the main sources of the increased mean flow losses and performance dispersion.

(3) By the Sobol method, the effects of each uncertainty on performance changes are quantified by sensitivities. The contributions of each inlet flow parameter variation to the changes in the total pressure-loss coefficient are almost the same. However, most of the changes in outlet flow angle and Zweifel number are attributed to the variation of inlet total pressure. For this LPT cascade, the contributions of the pairwise uncertainties to performance changes are quite different. The impact on performance changes may be strengthened or weakened, considering the effects of pairwise uncertainties.

Author Contributions: Conceptualization, W.F. and J.L.; Methodology, W.F.; Software, W.F., Z.C. and J.L.; Validation, W.F.; Formal Analysis, W.F., Z.C. and J.L.; Investigation, W.F.; Resources, W.F.; Data Curation, W.F.; Writing—Original Draft Preparation, W.F.; Writing—Review & Editing, J.L., Z.C. and W.F. All authors have read and agreed to the published version of the manuscript.

Funding: This research was funded by National Natural Science Foundation of China (Grant nos. 92152202, 51976183), National Science and Technology Major Project of China (Grant no. J2019-II-0012-0032).

Data Availability Statement: The data of the research is available from the corresponding author upon reasonable request.

Conflicts of Interest: The authors declare no conflict of interest.

Abbreviations

The following abbreviations are used in this manuscript:

ANN	artificial neural networks
ADGP	adaptive Gaussian process
CFD	computational fluid dynamics
GP	Gaussian process
LPT	low-pressure turbine
MM	method of moment
MAPE	mean absolute percentage error
MCS	Monte Carlo simulation
ML	machine learning
NIPC	non-intrusive polynomial chaos
PC	polynomial chaos
PDF	probability density function
RANS	Reynolds-averaged Navier–Stokes
UQ	uncertainty quantification

References

1. Montomoli, F.; Carnevale, M.; D'Ammaro, A.; Massini, M.; Salvadori, S. *Uncertainty Quantification in Computational Fluid Dynamics and Aircraft Engines*; Springer Briefs in Applied Sciences and Technology; Springer International Publishing: Cham, Switzerland, 2015.
2. Yao, J.; Gorrell, S.E.; Wadia, A.R. High-fidelity numerical analysis of per-rev-type inlet distortion transfer in multistage fans—Part I: Simulations with selected blade rows. *J. Turbomach.* **2010**, *132*, 041014. [CrossRef]
3. Ghisu, T.; Parks, G.; Jarrett, J.; Clarkson, P. Robust design optimization of gas turbine compression systems. *J. Propuls. Power* **2011**, *27*, 282–295. [CrossRef]
4. Luo, J.; Xia, Z.; Liu, F. Robust design optimization considering inlet flow angle variations of a turbine cascade. *Aerosp. Sci. Technol.* **2021**, *116*, 106893. [CrossRef]
5. Loeven, G.; Witteveen, J.; Bijl, H. Probabilistic collocation: An efficient non-intrusive approach for arbitrarily distributed parametric uncertainties. In Proceedings of the 45th AIAA Aerospace Sciences Meeting and Exhibit, Reno, NV, USA, 8–11 January 2007; p. 317.
6. Papadimitriou, D.I.; Papadimitriou, C. Aerodynamic shape optimization for minimum robust drag and lift reliability constraint. *Aerosp. Sci. Technol.* **2016**, *55*, 24–33. [CrossRef]
7. Ghanem, R.; Higdon, D.; Owhadi, H. *Handbook of Uncertainty Quantification*; Springer: Cham, Switzerland, 2017; Volume 6.
8. Putko, M.M.; Taylor III, A.C.; Newman, P.A.; Green, L.L. Approach for input uncertainty propagation and robust design in CFD using sensitivity derivatives. *J. Fluids Eng.* **2002**, *124*, 60–69. [CrossRef]
9. Luo, J.; Liu, F. Statistical evaluation of performance impact of manufacturing variability by an adjoint method. *Aerosp. Sci. Technol.* **2018**, *77*, 471–484. [CrossRef]
10. Xu, S.; Zhang, Q.; Wang, D.; Huang, X. Uncertainty Quantification of Compressor Map Using the Monte Carlo Approach Accelerated by an Adjoint-Based Nonlinear Method. *Aerospace* **2023**, *10*, 280. [CrossRef]
11. Najm, H.N. Uncertainty quantification and polynomial chaos techniques in computational fluid dynamics. *Annu. Rev. Fluid Mech.* **2009**, *41*, 35–52. [CrossRef]
12. Hosder, S.; Walters, R.; Balch, M. Efficient sampling for non-intrusive polynomial chaos applications with multiple uncertain input variables. In Proceedings of the 48th AIAA/ASME/ASCE/AHS/ASC Structures, Structural Dynamics, and Materials Conference, Honolulu, HI, USA, 23–26 April 2007; p. 1939.
13. Abraham, S.; Raisee, M.; Ghorbaniasl, G.; Contino, F.; Lacor, C. A robust and efficient stepwise regression method for building sparse polynomial chaos expansions. *J. Comput. Phys.* **2017**, *332*, 461–474. [CrossRef]

14. Guo, Z.; Chu, W.; Zhang, H. A data-driven non-intrusive polynomial chaos for performance impact of high subsonic compressor cascades with stagger angle and profile errors. *Aerosp. Sci. Technol.* **2022**, *129*, 107802. [CrossRef]
15. Chen, Z.; Xia, Z.; Luo, J. Impact of inlet flow angle variation on the performance of a transonic compressor blade using NIPC. *AIP Adv.* **2022**, *12*, 025001. [CrossRef]
16. Uncertainty Quantification in Turbomachinery Simulations. In Proceedings of the ASME Turbo Expo 2016: Turbomachinery Technical Conference and Exposition, Seoul, Republic of Korea, 13–17 June 2016.
17. Non-Deterministic CFD Simulation of a Transonic Compressor Rotor. In Proceedings of the ASME Turbo Expo 2009: Power for Land, Sea, and Air, Orlando, FL, USA, 8–12 June 2009.
18. Tang, X.; Wang, Z.; Xiao, P.; Peng, R.; Liu, X. Uncertainty quantification based optimization of centrifugal compressor impeller for aerodynamic robustness under stochastic operational conditions. *Energy* **2020**, *195*, 116930. [CrossRef]
19. Bishop, C.M. *Pattern Recognition and Machine Learning*; Information Science and Statistics; Springer: New York, NY, USA, 2006.
20. Hu, H.; Song, Y.; Yu, J.; Liu, Y.; Chen, F. The application of support vector regression and virtual sample generation technique in the optimization design of transonic compressor. *Aerosp. Sci. Technol.* **2022**, *130*, 107814. [CrossRef]
21. Wang, X.; Hirsch, C.; Liu, Z.; Kang, S.; Lacor, C. Uncertainty-based robust aerodynamic optimization of rotor blades. *Int. J. Numer. Methods Eng.* **2013**, *94*, 111–127. [CrossRef]
22. He, X.; Zheng, X. Performance improvement of transonic centrifugal compressors by optimization of complex three-dimensional features. *Proc. Inst. Mech. Eng. Part G J. Aerosp. Eng.* **2017**, *231*, 2723–2738. [CrossRef]
23. Cao, D.; Bai, G. A study on aeroengine conceptual design considering multi-mission performance reliability. *Appl. Sci.* **2020**, *10*, 4668. [CrossRef]
24. Zhang, Y.; Ghosh, S.; Pandita, P.; Subber, W.; Khan, G.; Wang, L. Remarks for scaling up a general gaussian process to model large dataset with sub-models. In Proceedings of the AIAA Scitech 2020 Forum, Orlando, FL, USA, 6–10 January 2020; p. 0678.
25. Krige, D.G. Some basic considerations in the application of geostatistics to the valuation of ore in South African gold mines. *J. South. Afr. Inst. Min. Metall.* **1976**, *76*, 383–391.
26. Hoef, J.M.V.; Cressie, N. Spatial Statistics: Analysis of Field Experiments. In *Design and Analysis of Ecological Experiments*; Oxford University Press: Oxford, UK, 2001.
27. O'Hagan, A. Curve fitting and optimal design for prediction. *J. R. Stat. Soc. Ser. B Methodol.* **1978**, *40*, 1–24. [CrossRef]
28. Sacks, J.; Welch, W.J.; Mitchell, T.J.; Wynn, H.P. Design and Analysis of Computer Experiments. *Stat. Sci.* **1989**, *4*, 409–423. [CrossRef]
29. Rasmussen, C.E.; Williams, C.K.I. *Gaussian Processes for Machine Learning*; Adaptive Computation and Machine Learning; MIT Press: Cambridge, MA, USA, 2006.
30. Lin, Q.; Hu, J.; Zhang, L.; Jin, P.; Cheng, Y.; Zhou, Q. Gradient-enhanced multi-output gaussian process model for simulation-based engineering design. *AIAA J.* **2022**, *60*, 76–91.
31. Kingma, D.P.; Ba, J. Adam: A Method for Stochastic Optimization. *arXiv* **2017**, arXiv:1412.6980.
32. Luo, J.; Fu, Z.; Zhang, Y.; Fu, W.; Chen, J. Aerodynamic optimization of a transonic fan rotor by blade sweeping using adaptive Gaussian process. *Aerosp. Sci. Technol.* **2023**, *137*, 108255. [CrossRef]
33. Zhou, Q.; Shao, X.; Jiang, P.; Gao, Z.; Wang, C.; Shu, L. An active learning metamodeling approach by sequentially exploiting difference information from variable-fidelity models. *Adv. Eng. Informatics* **2016**, *30*, 283–297. [CrossRef]
34. Cox, D.D.; Park, J.S.; Singer, C.E. A statistical method for tuning a computer code to a data base. *Comput. Stat. Data Anal.* **2001**, *37*, 77–92. [CrossRef]
35. Xia, Z.; Luo, J.; Liu, F. Performance impact of flow and geometric variations for a turbine blade using an adaptive NIPC method. *Aerosp. Sci. Technol.* **2019**, *90*, 127–139. [CrossRef]
36. Xia, Z.; Luo, J.; Liu, F. Statistical evaluation of performance impact of flow variations for a transonic compressor rotor blade. *Energy* **2019**, *189*, 116285. [CrossRef]
37. Mohammadi, A.; Shimoyama, K.; Karimi, M.S.; Raisee, M. Efficient uncertainty quantification of CFD problems by combination of proper orthogonal decomposition and compressed sensing. *Appl. Math. Model.* **2021**, *94*, 187–225. [CrossRef]
38. Sobol, I.M. Global sensitivity indices for nonlinear mathematical models and their Monte Carlo estimates. *Math. Comput. Simul.* **2001**, *55*, 271–280. [CrossRef]

Disclaimer/Publisher's Note: The statements, opinions and data contained in all publications are solely those of the individual author(s) and contributor(s) and not of MDPI and/or the editor(s). MDPI and/or the editor(s) disclaim responsibility for any injury to people or property resulting from any ideas, methods, instructions or products referred to in the content.